Chaos, Solitons and Fractals 211 (2026) 118791

Contents lists available at ScienceDirect

Chaos, Solitons and Fractals

journal homepage: www.elsevier.com/locate/chaos

Master stability in the presence of megastability: Emergence of oscillatory synchronization patterns

Karthikeyan Rajagopal [a,b], Arezoo Firouzeh [c], Mahtab Mehrabbeik [c], Sajad Jafari [c,d,*], Julien Clinton Sprott [e]

[a] Center for Research, Easwari Engineering College, Chennai, India
[b] Center for Research, SRM TRP Engineering College, Trichy, India
[c] Department of Biomedical Engineering, Amirkabir University of Technology (Tehran Polytechnic), Tehran, Iran
[d] Health Technology Research Institute, Amirkabir University of Technology (Tehran Polytechnic), Tehran, Iran
[e] Department of Physics, University of Wisconsin, Madison, WI 53706, USA

ARTICLE INFO

Keywords:
Megastability
Master stability function
Synchronization
Network

ABSTRACT

In this paper, we present the master stability function (MSF) analysis of synchronization in megastable dynamical systems—those with a countable infinity of coexisting attractors—across three benchmark oscillators (cabbage, simplest sinusoidal, and tanh–exponential) and four single coupling channels. For attractors selected by initial conditions, we quantify how dissipativity and external forcing shape stability on the synchronization manifold. While inner (more dissipative) attractors generally admit broader stability, the most striking outcome is the emergence of finely oscillatory MSF curves that partition the coupling axis into interleaved, narrow intervals. Unlike conventional MSF patterns, these repeated sign changes persist over wide coupling ranges, producing highly fragmented stability windows rather than a single contiguous region. This unprecedented phenomenon survives under forcing and depends strongly on the coupling pathway, revealing an unusually delicate balance between local megastable dynamics and network embedding. By characterizing this structured alternation of stable and unstable bands, the study clarifies why achieving collective synchrony in megastable regimes may be inherently challenging and points to targeted choices of attractor and coupling channel as key levers for future network designs.

1. Introduction

Synchronization is a fundamental collective phenomenon in nonlinear systems, where interacting units adjust their dynamics to operate in unison [1,2]. Originating from simple coupled oscillators, it now represents a universal mechanism observed in physics, biology, chemistry, and engineering, spanning from laser arrays to neuronal populations and power-grid models [1,3]. In recent years, advances in nonlinear electronic and neuromorphic circuits have further expanded the understanding of synchronization phenomena in physical implementations, illustrating how theoretical principles translate into practical applications [4–6]. Depending on coupling strength, topology, and intrinsic nonlinearity, networks can exhibit complete [7], phase [8], lag [9], or partial synchronization [10,11], each marking a distinct level of coherence across the units. These regimes may emerge, disappear, or coexist as parameters

* Corresponding author at: Department of Biomedical Engineering, Amirkabir University of Technology (Tehran Polytechnic), Tehran, Iran.
E-mail address: sajadjafari83@gmail.com (S. Jafari).

https://doi.org/10.1016/j.chaos.2026.118791
Received 30 May 2026; Received in revised form 2 July 2026; Accepted 4 July 2026
Available online 7 July 2026

vary, producing smooth transitions between states or sharp changes in collective behavior. In practice, the same network can traverse these forms of synchrony across operational ranges, shaping how coordinated activity is maintained in real-world systems.

In dynamical systems theory, synchronization occurs when the trajectories of coupled subsystems converge onto a common (invariant) manifold despite their intrinsic complexity [12]. The stability of this manifold—often quantified via the Master Stability Function (MSF)—determines whether small perturbations decay or grow [13]. MSF analysis has become a central topic in nonlinear dynamics and applied mathematics. Many studies have used the MSF to investigate how multilayer structures [14–16], higher-order interactions [17–19], coupling functions [20–22], and time-varying couplings [23–25] influence synchronization. In such settings, the MSF delineates the onset and parameter regions of stable synchrony, which is especially valuable in large networks. Complementary work has focused on the qualitative patterns of the MSF under specific configurations [26–28], offering mathematical insight into how architecture and node dynamics jointly shape stability.

Multistability is a hallmark of nonlinear dynamical systems, characterized by the coexistence of multiple stable attractors, such as fixed points, limit cycles, or chaotic states, under identical parameter conditions [29]. The system's long-term evolution depends on its initial state, meaning small perturbations can drive it toward entirely different behaviors. Two remarkable special cases of multistability are extreme multistability and megastability, each representing a unique manifestation of coexisting stable dynamics. In extreme multistability, an infinite continuum of attractors coexists, typically due to a conserved quantity or hidden invariant that creates a neutrally stable direction in phase space [30,31]. As a result, the final state varies continuously with initial conditions, forming a smooth manifold of possible attractors rather than discrete basins. In contrast, megastability refers to the coexistence of an infinite but discrete set of stable attractors, each with its own distinct basin of attraction [32–34]. These attractors are often arranged in a nested or lattice-like structure, arising from intrinsic invariances or modular nonlinearities in the system's equations. Unlike extreme multistability, where transitions between states are continuous, megastable systems exhibit abrupt switching between attractors as initial conditions cross basin boundaries. This discrete multiplicity of stable states makes megastability particularly intriguing for potential applications in information encoding, memory storage, and pattern formation within complex networks.

In megastable systems, the coexistence of infinitely many attractors adds a new layer of complexity: synchronization becomes attractor-dependent and can vary across coexisting states. Characterizing these differences reveals how complex networks self-organize, transition between order and chaos, and sustain coherence under competing dynamical influences. While conventional MSF behaviors in standard oscillators are well-classified into distinct categories based on their zero-crossing points and stability region (Classes Γ_0 to Γ_{IV}) [35], the highly oscillatory and severely fragmented MSF patterns with numerous, persistent zero-crossings have not been documented in the literature. Accordingly, this paper performs an MSF analysis for multiple coexisting solutions of three megastable oscillators, both with and without an external forcing term. Section 2 outlines the MSF framework; Section 3 presents detailed results for the three oscillators and their distinct attractor-dependent synchronization regimes; and Section 4 summarizes the key findings and implications.

2. Master stability analysis

Let $X_i \in \mathbb{R}^m$ denote the state of the i-the oscillator ($i = 1,\dots,N$). With intrinsic (node) dynamics $F : \mathbb{R}^m \to \mathbb{R}^m$ and a coupling function $H : \mathbb{R}^m \to \mathbb{R}^m$, the network evolves as

$$\dot{X}_i = F(X_i) + \sigma \sum_{j=1}^{N} a_{ij} H(X_j), \tag{1}$$

where $\sigma \in \mathbb{R}$ is the coupling strength and $A = [a_{ij}]_{N\times N}$ is a zero-row-sum adjacency matrix satisfying $a_{ii} = -\sum_{j\neq i} a_{ij}$. For a simple (unweighted) graph, $a_{ij} \in \{0,1\}$ for $i \neq j$, where $a_{ij} = 1$ indicate a connection between the nodes i and j and $a_{ij} = 0$ shows no connections.

For identical two-dimensional oscillators $X_i = [x_i, y_i]^T$ with and $F(X_i) = [f(X_i), g(X_i)]^T$, it is convenient to take linear selection $H(X_i) = CX_i$, where $C = \begin{bmatrix} c_{xx} & c_{yx} \\ c_{xy} & c_{yy} \end{bmatrix}$ specifies which component is broadcast into which equation. The common one-to-one component couplings are

- $x \to x$: $C = \begin{bmatrix} 1 & 0 \\ 0 & 0 \end{bmatrix} \Rightarrow H(X_j) = [x_j, 0]^T$
- $y \to x$: $C = \begin{bmatrix} 0 & 1 \\ 0 & 0 \end{bmatrix} \Rightarrow H(X_j) = [y_j, 0]^T$
- $x \to y$: $C = \begin{bmatrix} 0 & 0 \\ 1 & 0 \end{bmatrix} \Rightarrow H(X_j) = [0, x_j]^T$
- $y \to y$: $C = \begin{bmatrix} 0 & 0 \\ 0 & 1 \end{bmatrix} \Rightarrow H(X_j) = [0, y_j]^T$

This construction extends directly to three and higher dimensions by selecting the appropriate rows and columns of C.

In the synchronous state $X_1 = X_2 = \dots = X_N = X$, the network follows the isolated dynamics $\dot{X} = F(X)$, the coupling term vanishes by the zero-row-sum property: $\sum_{j=1}^{N} a_{ij} H(X) = H(X) \sum_{j=1}^{N} a_{ij} = 0$.

To assess the stability of this synchronous manifold, each node was perturbed by $\delta X_i = X_i - X$. Linearizing around X yields

$$\dot{\delta X_i} = JF(X)\delta X_i + \sigma \sum_{j=1}^{N} a_{ij} JH(X)\delta X_j, \tag{2}$$

where $JF(X)$ and $JH(X)$ are the Jacobians of F and H, both evaluated at X. Let $L = -A$ be the graph Laplacian and set $C = JH(X)$. Then

$$\dot{\delta X_i} = JF(X)\delta X_i - \sigma \sum_{j=1}^{N} l_{ij} C\delta X_j. \tag{3}$$

Since L is diagonalizable for undirected graphs (symmetric with an orthonormal eigenbasis), we can write $L = V\Lambda V^{-1}$ with eigenvalues $\Lambda = \{\lambda_1, \dots \lambda_N\}$. Projecting onto the Laplacian eigenmodes (denoting the modal perturbation by $\eta_i \mapsto \delta X_i$) gives the decoupled variational systems

$$\dot{\eta}_i = [JF(X) - K_i C]\eta_i, \tag{4}$$

where $K_i = \sigma\lambda_i$ is the normalized coupling strength.

Defining the MSF $\Psi(K)$ as the maximum Lyapunov exponent of System (4), the synchronous manifold is linearly stable if $\Psi(K) < 0$ for all transverse modes $i \geq 2$. For a connected graph, $\lambda_1 = 0$ corresponds to motion along the manifold; the onset of synchronization occurs when $\sigma\lambda_2$ first enters the interval $\{K_2 : \Psi(K_2) < 0\}$, while complete stability requires the entire spectrum $\{K_i : i > 0\}$ to lie inside that interval. Here, we evaluate the master-stability equation at $K \mapsto K_i$, yielding an MSF pattern that is independent of the network topology; the topology influences stability only through the Laplacian eigenvalues.

It is important to note that the standard MSF framework and the computation of Lyapunov exponents are rigorously defined for autonomous (time-invariant) dynamical systems. For the non-autonomous (externally forced) oscillators considered in this study, the Jacobian matrix explicitly depends on time. To resolve this and properly apply the standard MSF formulation, we introduce an auxiliary state variable (e.g., z with $\dot{z} = 1$) to embed the non-autonomous system into a higher-dimensional autonomous one. This transformation removes the explicit time dependence from the Jacobian, allowing the variational equations to be correctly decoupled and the Lyapunov exponents to be accurately computed. Crucially, since this auxiliary variable z represents universal time, it is identical across all oscillators in the network and does not participate in the coupling function; the coupling acts exclusively on the original physical state variables.

3. Results

We begin by assessing the linear stability of the synchronization manifold using the master-stability framework. In multistable settings, distinct initial conditions select different coexisting attractors; for each, we evaluate the corresponding MSF pattern. Our focus here is on megastable systems—a special case of multistability with an infinite, countable family of coexisting attractors—where we examine the synchronous solutions and compare their MSF patterns. This organization allows us to delineate, for each selected attractor, the parameter ranges that sustain synchronous behavior and to contrast stability characteristics across coexisting solutions.

In this paper, we use the term oscillatory MSF patterns to describe a specific phenomenological behavior of the MSF $\Psi(K)$ as a function of the coupling strength K. Unlike conventional MSF curves, which typically exhibit a single contiguous stable region or a monotonic trend, an oscillatory MSF pattern is characterized by repeated local maxima and minima in its shape. Mathematically, this oscillatory shape results in multiple zero-crossings, thereby fragmenting the synchronization stability into interleaved, narrow intervals of stable ($\Psi(K) < 0$) and unstable ($\Psi(K) > 0$) regimes.

It should be noted that all simulations are carried out using the fourth-order Runge–Kutta method with a time step of 0.005, over a total integration time of 10,000 time units, and a sampling resolution of 1000 points for the plotted diagrams. To select the specific coexisting attractors, the initial conditions are chosen from the basin of attraction of the synchronization manifold, which corresponds to the dynamics of the isolated system in each case. To compute the MSF, the maximum Lyapunov exponent of the variational equations was calculated using the standard Wolf algorithm [36]. The aforementioned integration time is sufficient to ensure that the trajectory settles onto the synchronization manifold and to guarantee the numerical convergence of the calculated exponents.

3.1. Case A: the cabbage oscillator

The term megastability was first introduced to describe a system exhibiting an infinite number of coexisting attractors arranged in layered structures, known as the cabbage system due to this characteristic. As the first case study, we consider the cabbage system, which is defined as follows [32]:

$$\begin{aligned} \dot{x} &= y, \\ \dot{y} &= -(0.33)^2 x + y\cos(x) + A\sin(0.73t) \end{aligned}. \tag{5}$$

Here, $X = [x, y]^T$ denotes the state vector, and A is a parameter controlling the amplitude of an additive forcing term. When $A = 0$, the system is time-independent and therefore autonomous; for $A \neq 0$, it becomes non-autonomous. Fig. 1a illustrates the first five inner coexisting attractors for $A = 0$, using the initial condition $X_0 = [x_0, 0]^T$ with $x_0 \in \{\pi, 3\pi, 5\pi, 7\pi, 9\pi\}$. As A increases, the dynamics become more complex and can exhibit additional solutions, with some attractors merging. For $A = 1$, Fig. 1b shows the coexisting attractors within the same x_0 domain—specifically $x_0 \in \{5\pi, 7\pi, 9\pi\}$. Here, the first three initial conditions $x_0 \in \{\pi, 3\pi, 5\pi\}$ converge to the same attractor (shown in red). In Fig. 2b, following the classification reported in [32], the two innermost attractors (shown in red and blue) exhibit chaotic dynamics, while the outer purple attractor corresponds to an attracting torus.

Letting $t \to z$ with $\dot{z} = 1$, System (5) (synchronization manifold) can be recast in autonomous form as:

$$\begin{aligned} \dot{x} &= y, \\ \dot{y} &= -(0.33)^2 x + y\cos(x) + A\sin(0.73z), \\ \dot{z} &= 1. \end{aligned} \tag{6}$$

For System (5), the Jacobian matrix in the synchronous state $X = (x, y, z)$ is

$$JF(X) = \begin{bmatrix} 0 & 1 & 0 \\ -(0.33)^2 - y\sin(x) & \cos(x) & 0.73A\cos(0.73z) \\ 0 & 0 & 0 \end{bmatrix}. \tag{7}$$

According to Eq. (4), the corresponding variational equations are

$$\begin{aligned} \dot{\eta}_x &= \eta_x - K[c_{xx}\eta_x + c_{yx}\eta_y], \\ \dot{\eta}_y &= -\left((0.33)^2 + y\sin(x)\right)\eta_x + \cos(x)\eta_y + 0.73A\cos(0.73z)\eta_z - K[c_{xy}\eta_x + c_{yy}\eta_y], \\ \dot{\eta}_z &= 0. \end{aligned} \tag{8}$$

Lyapunov analyses of System (8), or equivalently, the MSF $\Psi(K)$, for $A = 0$ and $0 \le K \le 10$, under the four one-to-one coupling configurations $x \to x$, $y \to x$, $x \to y$, and $y \to y$ are presented in Fig. 2a-d. Each colour shown in Fig. 2 corresponds to the same attractor colour depicted in Fig. 1a and is obtained using the identical initial conditions, i.e., $X_0 = [x_0, 0]^T$, $x_0 \in \{\pi, 3\pi, 5\pi, 7\pi, 9\pi\}$.

As shown in Fig. 2, $\Psi(0) = 0$, matching the maximum Lyapunov exponent of the isolated periodic/quasiperiodic dynamics. As K increases, synchronization is achieved immediately and maintained for the $x \to x$ (Fig. 2a) and $y \to y$ (Fig. 2d) couplings. The system's dissipation, quantified by the long-time average $\langle Trace(JF(X)) \rangle = \left\langle \frac{\partial \dot{x}}{\partial x} + \frac{\partial \dot{y}}{\partial y} + \frac{\partial \dot{z}}{\partial x} \right\rangle = \langle \cos(x) \rangle$, decreases as trajectories move farther from the origin. This reduction weakens synchronizability for $x \to x$ (Fig. 2a), where less dissipative manifolds (farther from the origin) exhibit smaller $|\Psi(K)|$. Under $y \to y$ (Fig. 2d) coupling, the effect persists but is mild, and the curves nearly coincide.

For $x \to y$ (Fig. 2c), the system remains broadly synchronizable, but zero-crossings appear for the less dissipative manifolds (red, blue, pink), whereas the inner manifolds (navy and green) stay stable over the entire K range. In contrast, for $y \to x$ (Fig. 2b) synchronization, if it occurs, appears only in narrow low-K windows near the first few lobes; beyond approximately $K \approx 4$, all curves satisfy $\Psi(K) > 0$, indicating loss of synchrony. Moreover, the less dissipative manifolds exhibit smaller or no stable windows and larger positive Ψ. Finally, Fig. 2c shows an attractor-specific minimum Ψ_{min} for each curve, an empirical feature not captured analytically.

Fig. 3 reports the master-stability analysis of System (6) with $A = 1$ over $0 \le K \le 10$ for four coupling configurations. As in the unforced case, dissipation decreases as the attractors (manifolds) move farther from the origin. The long-time average dissipation rates before ($A = 0$) and after ($A = 1$) are listed in Table 1, confirming that the system becomes less dissipative under forcing. The MSF trends in Fig. 3 are largely preserved relative to Fig. 2: the $x \to x$ (panel a), $y \to y$ (panel d), and $y \to x$ (panel b) couplings show similar patterns and stability behavior In contrast, under the $x \to y$ coupling (panel c), numerous zero crossings emerge—most prominently for the innermost manifold (red), indicating intermittent transitions between stable and unstable synchronization intervals.

For better clarity, Fig. 4 illustrates the MSF pattern corresponding to the innermost attractor of the cabbage oscillator—the red curves in Figs. 1 and 3—under the forcing term with $A = 1$ over two coupling ranges: $K \in [0, 10]$ (panel a) and $K \in [0, 100]$ (panel b). This figure reveals that numerous stability transitions occur for $K \lesssim 10$; however, as K increases, the manifold stabilizes and maintains a negative $\Psi(K)$, indicating that synchronization is achievable for $K > 10$. Furthermore, similar to Fig. 2c, the MSF curve exhibits a specific minimum value Ψ_{min}, which cannot be determined analytically.

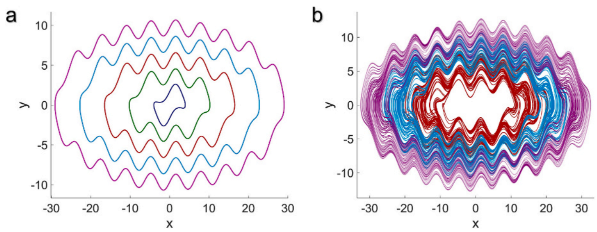

Fig. 1. Coexisting attractors of the megastable cabbage oscillator (System 5) projected onto the x-y plane. **(a)** Autonomous case ($A = 0$) showing the first five nested attractors obtained with initial conditions $X_0 = [x_0, 0]^T$ for $x_0 \in \{\pi, 3\pi, 5\pi, 7\pi, 9\pi\}$, The attractors exhibit a layered, "cabbage-like" structure. **(b)** Forced case ($A = 1$) with initial conditions $X_0 = [x_0, 0]^T$ for $x_0 \in \{5\pi, 7\pi, 9\pi\}$. The forcing term enriches the dynamics, resulting in the coexistence of chaotic (red and blue) and quasiperiodic/torus (purple) attractors, and causes the merging of the three innermost attractors from the unforced case into a single chaotic attractor (red). (For interpretation of the references to colour in this figure legend, the reader is referred to the web version of this article.)

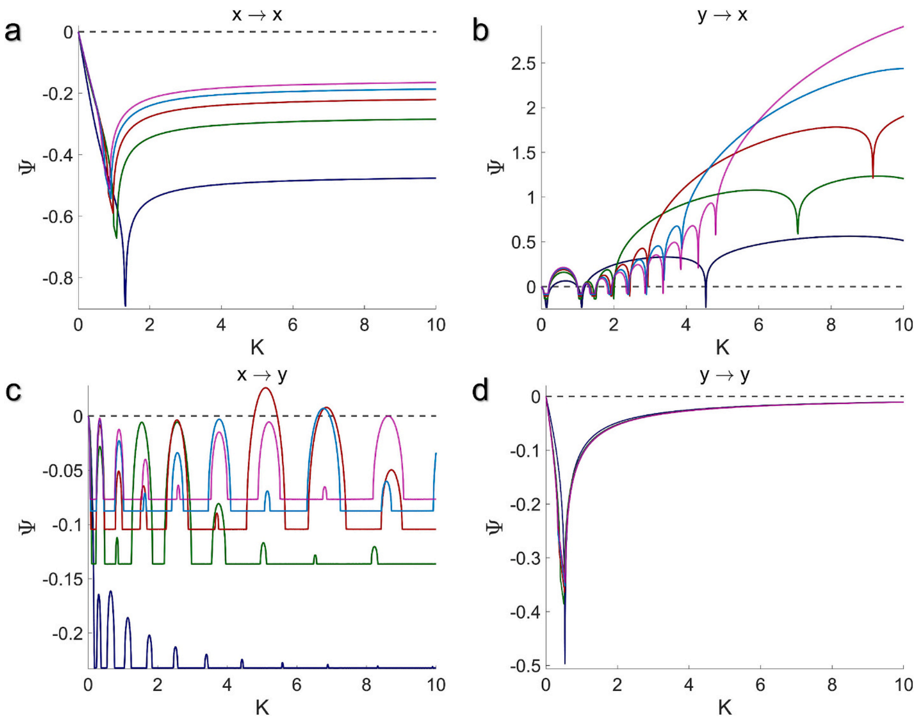

Fig. 2. MSF, defined as the maximum transverse Lyapunov exponent $\Psi(K)$, for the autonomous cabbage oscillator (variational System 8, $A = 0$) over the normalized coupling strength range $0 \le K \le 10$. The four panels correspond to the four single-variable coupling configurations: **(a)** $x \rightarrow x$, **(b)** $y \rightarrow x$, **(c)** $x \rightarrow y$, and **(d)** $y \rightarrow y$. Each colored curve represents the MSF evaluated on a specific coexisting attractor (synchronization manifold) selected by the initial conditions $X_0 = [x_0, 0]^T$, with $x_0 \in \{\pi, 3\pi, 5\pi, 7\pi, 9\pi\}$, matching the colors of the attractors in Fig. 1a. The plots reveal that inner (more dissipative) attractors generally exhibit broader stability regions, and the choice of coupling channel critically determines the width and existence of these stable windows.

3.2. Case B: the simplest sinusoidal megastable oscillator

As the second case study, we consider the simplest megastable oscillator with a single sinusoidal nonlinearity [33]. Using the same notation as before, the original two-dimensional system is

$$\begin{aligned} &\dot{x} = -y, \\ &\dot{y} = 0.1x + \sin(y) + A\sin(0.7t). \end{aligned} \tag{9}$$

By introducing $t \rightarrow z$ and $\dot{z} = 1$, the system is recast in autonomous form:

$$\begin{aligned} &\dot{x} = -y, \\ &\dot{y} = 0.1x + \sin(y) + A\sin(0.7z), \\ &\dot{z} = 1, \end{aligned} \tag{10}$$

where z serves as the time-like state.

Considering the autonomous form of System (10) as the dynamics on the synchronization manifold, the Jacobian along the synchronous trajectory $X = (x, y, z)$ is

$$JF(X) = \begin{bmatrix} 0 & -1 & 0 \\ 0.1 & \cos(y) & 0.7A\cos(0.7z) \\ 0 & 0 & 0 \end{bmatrix}. \tag{11}$$

Accordingly, based on Eq. (4), the variational equations are

$$\begin{aligned} &\dot{\eta}_x = -\eta_y - K\left[c_{xx}\eta_x + c_{yx}\eta_y\right], \\ &\dot{\eta}_y = 0.1\eta_x + \cos(y)\eta_y + 0.7A\sin(0.7z)\eta_z - K\left[c_{xy}\eta_x + c_{yy}\eta_y\right], \\ &\dot{\eta}_z = 0. \end{aligned} \tag{12}$$

Fig. 5 illustrates the dynamics of the five innermost attractors of System (9) for $A = 0$ (autonomous case; panel a) and $A = 0.85$ (non-autonomous case; panel b), using the initial conditions $X = [x_0, 0]^T$ with $x_0 \in \{16, 32, 52, 72, 92\}$. For each selected x_0 a distinct attractor is obtained in both panels, and—unlike in Case A—no attractor merging occurs after introducing the forcing term. In the

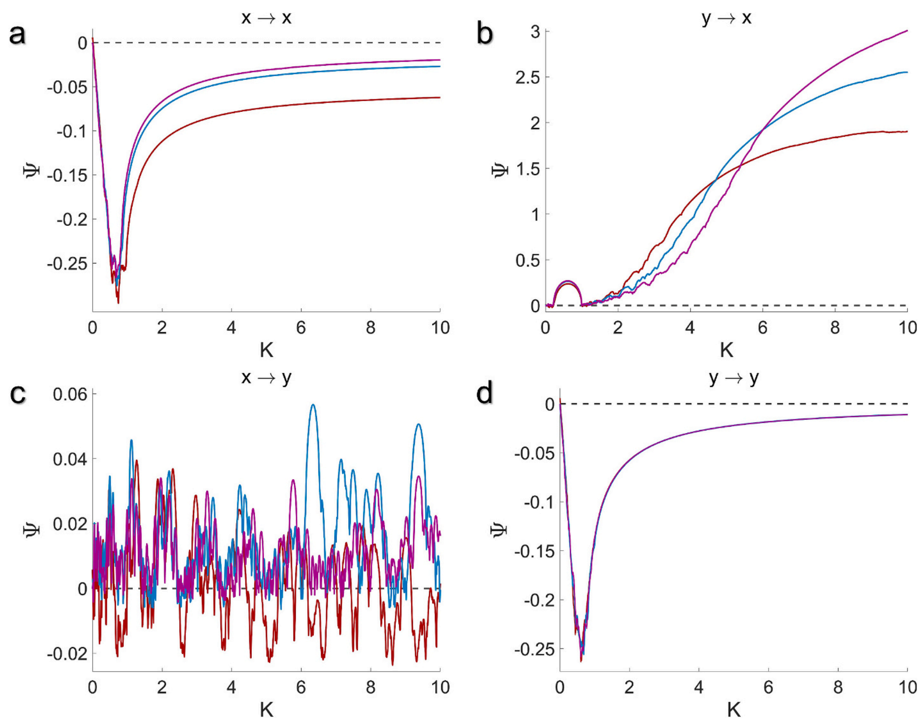

Fig. 3. MSF, defined as the maximum transverse Lyapunov exponent $\Psi(K)$, for the forced cabbage oscillator (variational System 8, $A = 1$) over the normalized coupling strength range $0 \le K \le 10$. The four panels correspond to the four single-variable coupling configurations: **(a)** $x \to x$, **(b)** $y \to x$, **(c)** $x \to y$, and **(d)** $y \to y$. Each colored curve represents the MSF evaluated on a specific coexisting attractor (synchronization manifold) selected by the initial conditions $X_0 = [x_0, 0]^T$, with $x_0 \in \{5\pi, 7\pi, 9\pi\}$, matching the colors of the attractors in Fig. 1b. Compared to the unforced case (Fig. 2), the external forcing preserves the general stability trends for $x \to x$, $y \to x$, and $y \to y$ couplings. However, under the $x \to y$ coupling (panel c), the forcing induces numerous zero-crossings, particularly for the innermost manifold, indicating intermittent transitions between stable and unstable synchronization intervals.

Table 1
Long-time average dissipation rate, calculated as $\langle Trace(JF(X)) \rangle = \langle cos(x) \rangle$, for the cabbage oscillator (System 5) before ($A = 0$) and after ($A = 1$) introducing the external forcing term. The values are reported for the coexisting attractors selected by different initial conditions $[x_0, y_0]$. The negative values indicate dissipative dynamics, and the trend shows that outer attractors (larger x_0) are less dissipative. Introducing the forcing term ($A = 1$) significantly reduces the overall dissipation rate, making the system's dynamics less dissipative on average.

Forcing amplitude	Initial setting $[\boldsymbol{x_0}, \boldsymbol{y_0}]$	Dissipation rate $\langle \boldsymbol{Trace}(\boldsymbol{JF}(\boldsymbol{X})) \rangle$
$\boldsymbol{A} = \mathbf{0}$	$[\pi, 0]$	-0.4643
	$[3\pi, 0]$	-0.2729
	$[5\pi, 0]$	-0.2088
	$[7\pi, 0]$	-0.1751
	$[9\pi, 0]$	-0.1537
$\boldsymbol{A} = \mathbf{1}$	$[5\pi, 0]$	-0.0522
	$[7\pi, 0]$	-0.0153
	$[9\pi, 0]$	-0.0081

unforced system (panel a), the phase portraits form a strictly nested family of smooth closed curves, each corresponding to a period-1 limit cycle whose amplitude increases monotonically with $|x_0|$. When the forcing is applied (panel b), the hierarchy is retained, but the dynamics become richer: the innermost response (navy) exhibits chaotic motion; it is encircled by a period-3 orbit (green), and these are enclosed by nested quasiperiodic trajectories (red, blue, and pink) associated with invariant tori. Collectively, the figure shows a one-to-one correspondence between the chosen initial conditions and the realized attractors, while highlighting the transition from purely periodic behavior in the autonomous case to a mixture of chaotic, periodic, and quasiperiodic motions under forcing.

Considering $A = 0$, Fig. 6 presents the Lyapunov analysis of System (12) for each attractor (representing the synchronization manifold) shown in Fig. 5a, under the four one-to-one coupling configurations: $x \to x$ (panel a), $y \to x$ (panel b), $x \to y$ (panel c), and $y \to y$ (panel d) within the range $0 \le K \le 10$. Overall, the results indicate that synchronization is attainable for all positive K values in the $x \to x$, $y \to x$, and $y \to y$ configurations, though the specific stability trends differ. The dissipation analysis (see Table 2), similar to that in

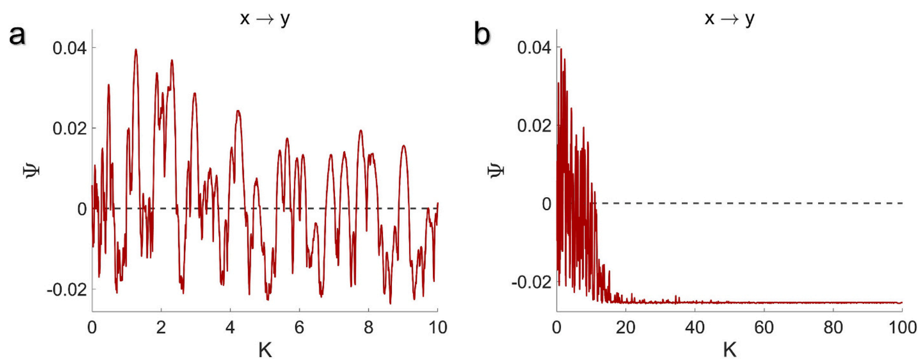

Fig. 4. Extended analysis of the MSF $\Psi(K)$ for the innermost attractor (red curve in Fig. 1b) of the forced cabbage oscillator (variational System 8, $A = 1$) under the $x \to y$ coupling configuration. The plots show $\Psi(K)$ over two different coupling ranges: **(a)** $0 \leq K \leq 10$ and **(b)** $0 \leq K \leq 100$. The initial condition used is $X_0 = [5\pi, 0]^T$. This extended view reveals that while numerous stability transitions (zero-crossings) occur for $K \lesssim 10$, the MSF curve eventually settles into a negative baseline for $K > 10$, indicating that stable synchronization is ultimately achievable at sufficiently high coupling strengths. The presence of a specific minimum value, Ψ_{min}, highlights the asymptotic stabilization of the manifold. (For interpretation of the references to colour in this figure legend, the reader is referred to the web version of this article.)

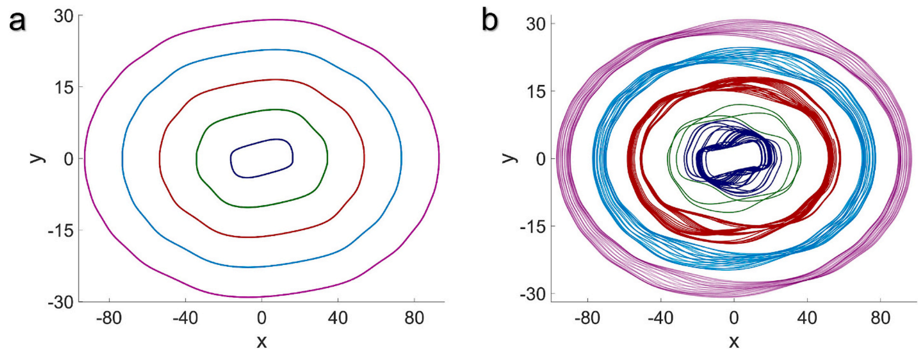

Fig. 5. Coexisting attractors of the simplest sinusoidal megastable oscillator (System 9) projected onto the x-y plane. **(a)** Autonomous case ($A = 0$) showing the five innermost nested period-1 limit cycles obtained with initial conditions $X_0 = [x_0, 0]^T$ for $x_0 \in \{16, 32, 52, 72, 92\}$. (b) Forced case ($A = 0.85$) with the same initial conditions. Unlike the cabbage oscillator, introducing the forcing term does not cause attractor merging; instead, it enriches the dynamics. The innermost response becomes chaotic (navy), a surrounding period-3 orbit emerges (green), and the outer trajectories become quasiperiodic invariant tori (red, blue, and pink). (For interpretation of the references to colour in this figure legend, the reader is referred to the web version of this article.)

Case A, shows a gradual reduction in dissipativity for outer attractors. This decline influences the synchronization stability: in the $x \to x$ (Fig. 6a), $|\Psi(K)|$ decreases for outer manifolds, signifying weaker stability farther from the origin. A similar but milder trend appears under $y \to y$ (Fig. 6d), where the curves exhibit comparable shapes but smaller variations. In both cases, the stability decays approximately exponentially with K, albeit with different rates of decline.

For the $y \to x$ configuration (Fig. 6b), the stability curves display oscillatory patterns with several loops, yet they remain entirely below the zero line, meaning the synchronous state persists despite the modulations. The baseline of these oscillations shifts closer to zero for outer attractors, consistent with the lower dissipativity observed. In contrast, under $x \to y$ coupling (Fig. 6c), synchronization cannot be sustained except for a narrow interval at small K values. This interval is practically negligible and would vanish in networks where the Laplacian eigenvalues are widely spread. Notably, even when $\Psi(K)$ remains positive, the qualitative trend of the MSF curves is preserved across all attractors, reflecting a consistent dynamical response structure.

Based on the values in Table 2, the system's dissipativity, defined as $\langle Trace(JF(X)) \rangle = \langle \cos(y) \rangle$, decreases markedly when the forcing term is applied, even though the dynamics become richer and more complex. Fig. 7 presents the master-stability analysis for $A = 0.85$. Comparing Figs. 6 and 7 shows that the MSF patterns are essentially preserved for $x \to x$ (panel a), $x \to y$ (panel c), and $y \to y$ (panel d): in $x \to x$ and $y \to y$, the curves remain strictly negative over $0 \leq K \leq 10$ (synchronizable throughout), whereas in $x \to y$ they remain strictly positive (unsynchronizable almost throughout). In contrast, with $y \to x$ coupling (panel b), the MSF changes substantially—oscillatory lobes introduce zero crossings, producing alternating stable/unstable K intervals. The baseline level of $\Psi(K)$ is consistent with the dissipation trend, but the detailed pattern is not. For example, the green curve—corresponding to the period-3 attractor in Fig. 5b—attains the largest positive Ψ over several K ranges and thus generates multiple zero crossings.

Fig. 8 illustrates the variation of $\Psi(K)$ for the $y \to x$coupling configuration, computed using the initial condition $X_0 = [x_0, y_0]^T =$

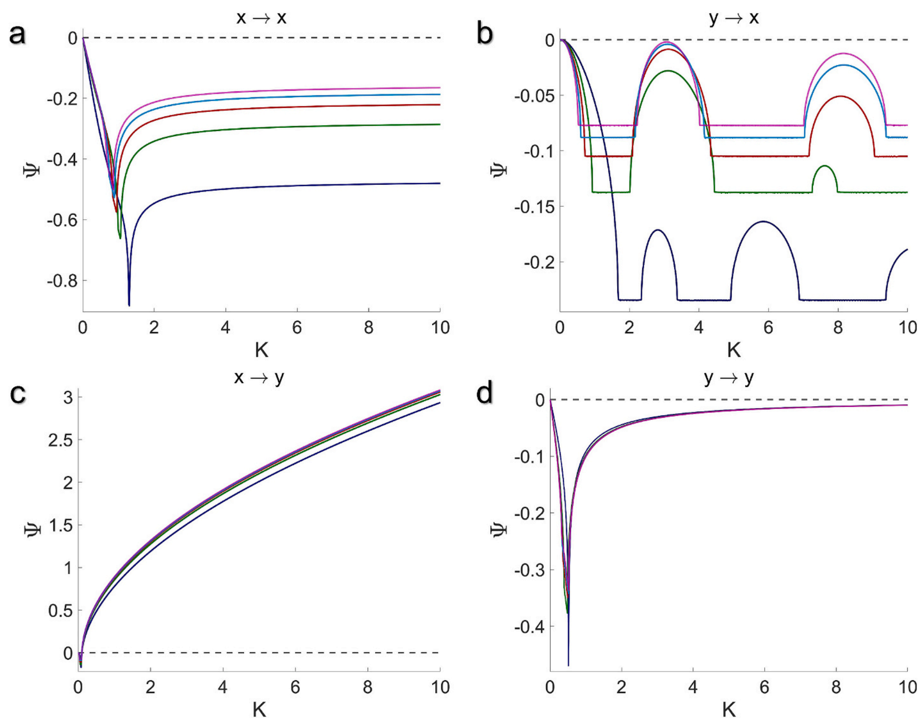

Fig. 6. MSF, defined as the maximum transverse Lyapunov exponent $\Psi(K)$, for the autonomous simplest sinusoidal oscillator (variational System 12, $A = 0$) over the normalized coupling strength range $0 \leq K \leq 10$. The four panels correspond to the four single-variable coupling configurations: **(a)** $x \rightarrow x$, **(b)** $y \rightarrow x$, **(c)** $x \rightarrow y$, and **(d)** $y \rightarrow y$. Each colored curve represents the MSF evaluated on a specific coexisting attractor (synchronization manifold) selected by the initial conditions $X_0 = [x_0, 0]^T$, with $x_0 \in \{16, 32, 52, 72, 92\}$, matching the colors of the attractors in Fig. 5a. Synchronization is broadly attainable for positive K in the $x \rightarrow x$, $y \rightarrow x$, and $y \rightarrow y$ configurations, though stability weakens for outer (less dissipative) manifolds. Notably, under $x \rightarrow y$ coupling (panel c), synchronization is largely unsustainable except for a negligible interval at very small K.

Table 2
Long-time average dissipation rate, calculated as $\langle Trace(JF(X)) \rangle = \langle cos(y) \rangle$, for the simplest sinusoidal oscillator (System 9) before ($A = 0$) and after ($A = 0.85$) introducing the external forcing term. The values are reported for the coexisting attractors selected by different initial conditions $[x_0, y_0]$. Similar to the cabbage oscillator, outer attractors exhibit lower dissipation rates. The application of the forcing term significantly reduces the overall dissipation, indicating that the richer, more complex dynamics induced by forcing are accompanied by a decrease in the system's average dissipativity.

Forcing amplitude	Initial setting $[\boldsymbol{x_0}, \boldsymbol{y_0}]$	Dissipation rate $\langle \boldsymbol{Trace}(\boldsymbol{JF}(\boldsymbol{X})) \rangle$
$\boldsymbol{A} = \mathbf{0}$	[16, 0]	−0.4694
	[32, 0]	−0.2749
	[52, 0]	−0.2098
	[72, 0]	−0.1757
	[92, 0]	−0.1540
$\boldsymbol{A} = \mathbf{0.85}$	[16, 0]	−0.2348
	[32, 0]	−0.1110
	[52, 0]	−0.0945
	[72, 0]	−0.0847
	[92, 0]	−0.0759

$[32, 0]^T$, which corresponds to the green period-3 attractor in Fig. 5b. Fig. 8a shows the results over $0 \leq K \leq 10$, while Fig. 8b extends the range to $0 \leq K \leq 100$. The plots reveal that several zero-crossing points occur for $K \lesssim 30$, where the oscillatory lobes of the MSF curve repeatedly intersect the zero line, leading to alternating stability and instability intervals. For $K > 30$, the amplitude of these lobes diminishes significantly, and no further zero crossings are observed, indicating that the system settles into a stable synchronization regime. Additionally, a minimum baseline value, Ψ_{min}, can be identified, which becomes more evident at larger K values, highlighting the asymptotic stabilization of the synchronization manifold.

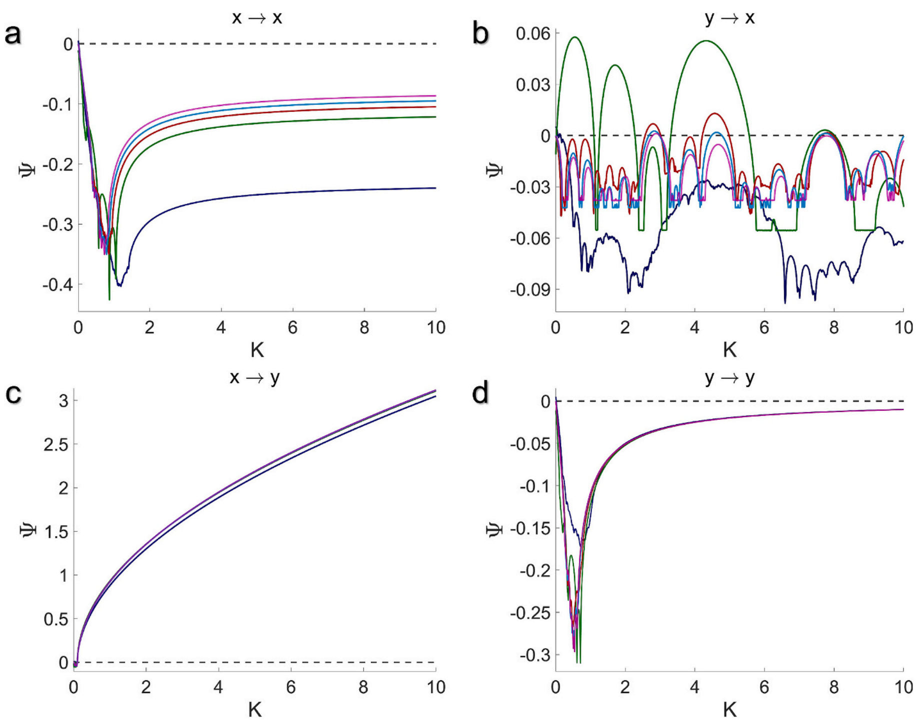

Fig. 7. MSF, defined as the maximum transverse Lyapunov exponent $\Psi(K)$, for the forced simplest sinusoidal oscillator (variational System 12, $A = 0.85$) over the normalized coupling strength range $0 \leq K \leq 10$. The four panels correspond to the four single-variable coupling configurations: **(a)** $x \to x$, **(b)** $y \to x$, **(c)** $x \to y$, and **(d)** $y \to y$. Each colored curve represents the MSF evaluated on a specific coexisting attractor (synchronization manifold) selected by the initial conditions $X_0 = [x_0, 0]^T$, with $x_0 \in \{16, 32, 52, 72, 92\}$, matching the colors of the attractors in Fig. 5b. Comparing with the unforced case (Fig. 6), the MSF patterns are largely preserved for $x \to x$, $x \to y$, and $y \to y$ couplings. However, under the $y \to x$ coupling (panel b), the forcing introduces substantial changes: the previously stable oscillatory lobes now cross the zero line, producing alternating stable and unstable synchronization intervals, with the period-3 attractor (green) exhibiting the most pronounced instability. (For interpretation of the references to colour in this figure legend, the reader is referred to the web version of this article.)

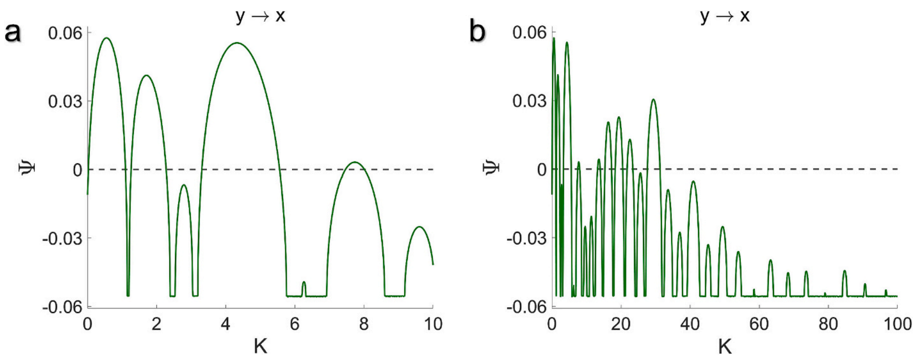

Fig. 8. Extended analysis of the MSF $\Psi(K)$ for the period-3 attractor (green curve in Fig. 5b) of the forced simplest sinusoidal oscillator (variational System 12, $A = 0.85$) under the $y \to x$ coupling configuration. The plots show $\Psi(K)$ over two different coupling ranges: **(a)** $0 \leq K \leq 10$ and **(b)** $0 \leq K \leq 100$. The initial condition used is $X_0 = [32, 0]^T$. The extended range reveals that while the MSF curve exhibits multiple zero-crossings and oscillatory lobes for $K \lesssim 30$, the amplitude of these oscillations diminishes significantly for $K > 30$. The curve eventually settles below the zero line, indicating asymptotic stabilization of the synchronization manifold at sufficiently high coupling strengths. (For interpretation of the references to colour in this figure legend, the reader is referred to the web version of this article.)

3.3. *Case C: a mixed tanh–exponential megastable system*

As the third and final case, we consider a system with both hyperbolic-tangent and exponential nonlinearities, capable of exhibiting two classes of attractors at small and large spatial scales [34]. The non-autonomous formulation is

$$\dot{x} = \tanh(y),$$
$$\dot{y} = -0.09x + y\cos(x) + x\exp\left(\frac{(x-30)^2}{5}\right)\tanh(x) + A\sin\left(\sqrt{3}\,t\right) \tag{13}$$

Introducing $t \to z$ with $\dot{z} = 1$ yields the autonomous form

$$\dot{x} = \tanh(y),$$
$$\dot{y} = -0.09x + y\cos(x) + x\exp\left(-\frac{(x-30)^2}{5}\right)\tanh(x) + A\sin\left(\sqrt{3}\,z\right), \tag{14}$$
$$\dot{z} = 1.$$

Treating System (14) as the dynamics on the synchronization manifold, the Jacobian along a synchronous trajectory $X = (x, y, z)$ is

$$JF(X) = \begin{bmatrix} 0 & \mathrm{sech}^2(y) & 0 \\ \rho & \cos(x) & \sqrt{3}\,A\cos\left(\sqrt{3}\,z\right) \\ 0 & 0 & 0 \end{bmatrix}, \tag{15}$$

where

$$\rho = -0.09 - y\sin(x) + \exp\left(-\frac{(x-30)^2}{5}\right)\left[\tanh(x) - \left(\frac{2x(x-30)}{5}\right)\tanh(x) + x\,\mathrm{sech}^2(x)\right].$$

According to Eq. (4), the variational equations are

$$\dot{\eta}_x = \mathrm{sech}^2(y)\eta_y - K\left[c_{xx}\eta_x + c_{yx}\eta_y\right],$$
$$\dot{\eta}_y = \rho\eta_x + \cos(x)\eta_y + \sqrt{3}A\cos\left(\sqrt{3}\,z\right)\eta_z - K\left[c_{xy}\eta_x + c_{yy}\eta_y\right], \tag{16}$$
$$\dot{\eta}_z = 0.$$

For $A = 0$ (autonomous version), the four innermost attractors of System (13), obtained with initial conditions $X_0 = [x_0, 0]^T$ with $x_0 \in \{2, 10, 15, 25\}$, are shown in Fig. 9a. These attractors form smooth, symmetric, and closed trajectories that correspond to period-1 oscillations, with amplitude increasing gradually as x_0 grows. When the forcing term is introduced ($A = 2.7$), as illustrated in Fig. 9b, the system's qualitative behavior changes significantly. The inner trajectories develop irregular distortions and folding, indicating the onset of chaotic motion, while the outer attractors broaden into multi-loop structures with quasiperiodic/chaotic features. Overall, the forcing term enriches the system dynamics, introducing a coexistence of regular and chaotic regimes that reflect the strong interplay between the tanh and exponential nonlinearities.

Fig. 10 presents the MSF $\Psi(K)$ for the variational System (16) associated with the attractors in Fig. 9a ($A = 0$) over $0 \le K \le 10$. Under $x \to x$ coupling (panel a), all curves remain strictly negative across the range, so the synchronous state is stable; stability is strongest for the innermost attractor (navy) and weakens outward, as indicated by smaller $|\Psi(K)|$ for the green, red, and blue curves. For $y \to x$ (panel b), $\Psi(K)$ is positive over most of the interval with only narrow dips below zero, implying that synchronization is generally not sustained. With $y \to y$ coupling (panel d), the curves start negative but cross the zero line at a finite K and remain slightly positive thereafter; thus, any synchrony is confined to a narrow low-K window near the origin, and for larger K the MSF is positive and synchronization is not achievable.

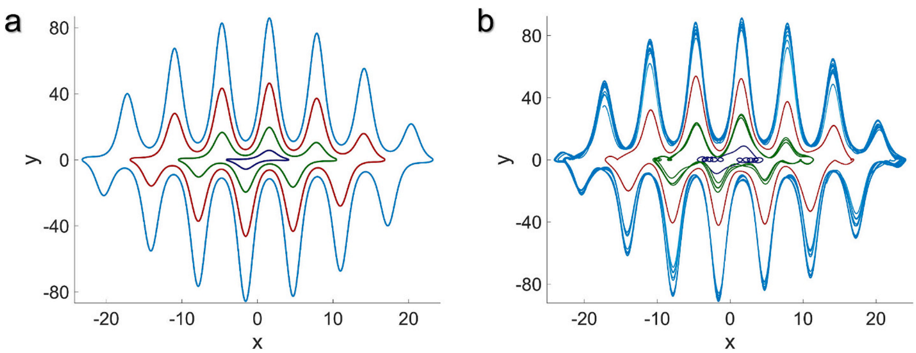

Fig. 9. Coexisting attractors of mixed tanh–exponential megastable system (System 13) projected onto the x-y plane. **(a)** Autonomous case ($A = 0$) showing the four innermost smooth, symmetric period-1 limit cycles obtained with initial conditions $X_0 = [x_0, 0]^T$ for $x_0 \in \{2, 10, 15, 25\}$. **(b)** Forced case ($A = 2.7$) with the same initial conditions. The introduction of the forcing term significantly alters the qualitative behavior: the inner trajectories develop irregular distortions indicating chaotic motion, while the outer attractors broaden into multi-loop structures exhibiting quasi-periodic and chaotic features.

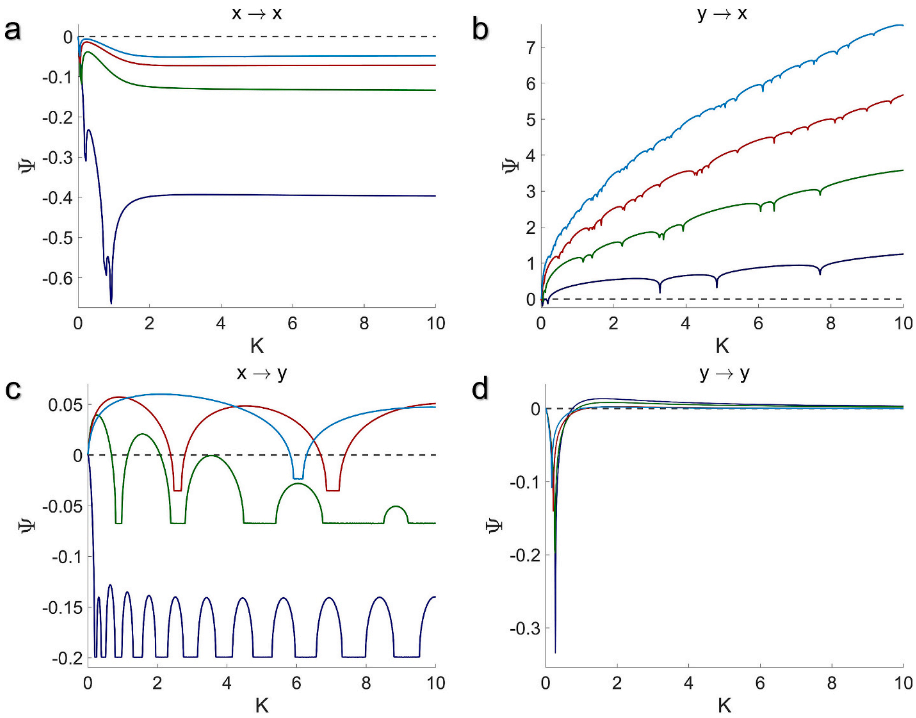

Fig. 10. MSF, defined as the maximum transverse Lyapunov exponent $\Psi(K)$, for the autonomous mixed tanh–exponential oscillator (variational System 16, $A = 0$) over the normalized coupling strength range $0 \le K \le 10$. The four panels correspond to the four single-variable coupling configurations: **(a)** $x \to x$, **(b)** $y \to x$, **(c)** $x \to y$, and **(d)** $y \to y$. Each colored curve represents the MSF evaluated on a specific coexisting attractor (synchronization manifold) selected by the initial conditions $X_0 = [x_0, 0]^T$, with $x_0 \in \{2, 10, 15, 25\}$, matching the colors of the attractors in Fig. 9a. The plots show that under $x \to x$ coupling, all attractors are synchronizable, with stability weakening outward. Under $y \to x$ and $y \to y$ couplings, synchronization is largely unattainable or confined to very narrow low-K windows. The $x \to y$ coupling (panel c) exhibits alternating stability windows, heavily dependent on the specific attractor.

The $x \to y$ case (panel c) shows alternating stability windows: the innermost (navy) curve is negative throughout; the green curve stays negative with shallow plateaus; the red and blue curves are predominantly positive but cross below zero in limited K intervals near the prominent lobes. Consistent with Table 3, outer attractors are less dissipative, which appears as reduced stability (curves closer to zero) in the stable configurations and as a higher positive baseline in the unstable ones.

Unlike the two previous cases, introducing the forcing term here almost increases dissipativity, quantified by $\langle Trace(JF(X)) \rangle = \langle \cos(x) \rangle$. Fig. 11 reports the master-stability analysis for $A = 2.7$ across the four coupling configurations. The overall trends are largely preserved: under $x \to x$ (panel a), the curves remain strictly negative over $0 \le K \le 10$ (robust synchronizability), and under $y \to x$ (panel b), they remain strictly positive (no synchrony). With $y \to y$ coupling (panel d), the MSF is initially negative for small K, indicating a short region of stability. However, as K increases, all curves cross the zero line and become positive, gradually approaching zero from above. This shows that synchronization is only possible in a narrow low-K interval, while for larger K values the system loses stability and synchronization cannot be achieved.

The most pronounced change appears in the $x \to y$ configuration (panel c). Stability windows shrink markedly: the innermost manifold (navy) develops a broad positive lobe—becoming unstable over a finite K interval, while the other manifolds (green, red, blue) show enlarged positive regions and fewer/shallower negative dips. In short, forcing degrades synchronizability for $x \to y$ configuration, while leaving the qualitative behavior of the other couplings essentially unchanged.

A closer inspection of the red curve in Fig. 11c, corresponding to the third attractor in Fig. 9b, is provided in Fig. 12a for clarity. This MSF pattern exhibits several zero-crossing points within the interval $0 \le K \le 10$, suggesting intermittent transitions between stable and unstable regions. To verify whether these oscillations persist or decay with increasing K, the analysis was extended to $0 \le K \le 100$, as shown in Fig. 12b. Unlike the previous cases, the MSF pattern here maintains its oscillatory structure over the entire range, with numerous lobes and frequent zero-crossing points, rather than damping toward a negative baseline. This behavior indicates that the synchronization manifold remains highly sensitive to variations in coupling strength. Since the stability windows are extremely narrow and scattered, the system is effectively unsynchronizable, particularly in networks where the Laplacian eigenvalue spectrum spans a broad range.

Table 3
Long-time average dissipation rate, calculated as $\langle Trace(JF(X))\rangle = \langle cos(x)\rangle$, for the mixed tanh–exponential oscillator (System 13) before ($A = 0$) and after ($A = 2.7$) introducing the external forcing term. The values are reported for the coexisting attractors selected by different initial conditions $[x_0, y_0]$. Unlike the previous two cases, introducing the forcing term in this system slightly increases the overall dissipation rate (making it more negative), although outer attractors consistently remain less dissipative than inner ones.

Forcing amplitude	Initial setting $[\boldsymbol{x_0}, \boldsymbol{y_0}]$	Dissipation rate $\langle \boldsymbol{Trace}(\boldsymbol{JF}(\boldsymbol{X}))\rangle$
$\boldsymbol{A} = \mathbf{0}$	$[2, 0]$	-0.3986
	$[10, 0]$	-0.1356
	$[15, 0]$	-0.0711
	$[25, 0]$	-0.0474
$\boldsymbol{A} = \mathbf{2.7}$	$[2, 0]$	-0.4530
	$[10, 0]$	-0.1501
	$[15, 0]$	-0.0885
	$[25, 0]$	-0.0451

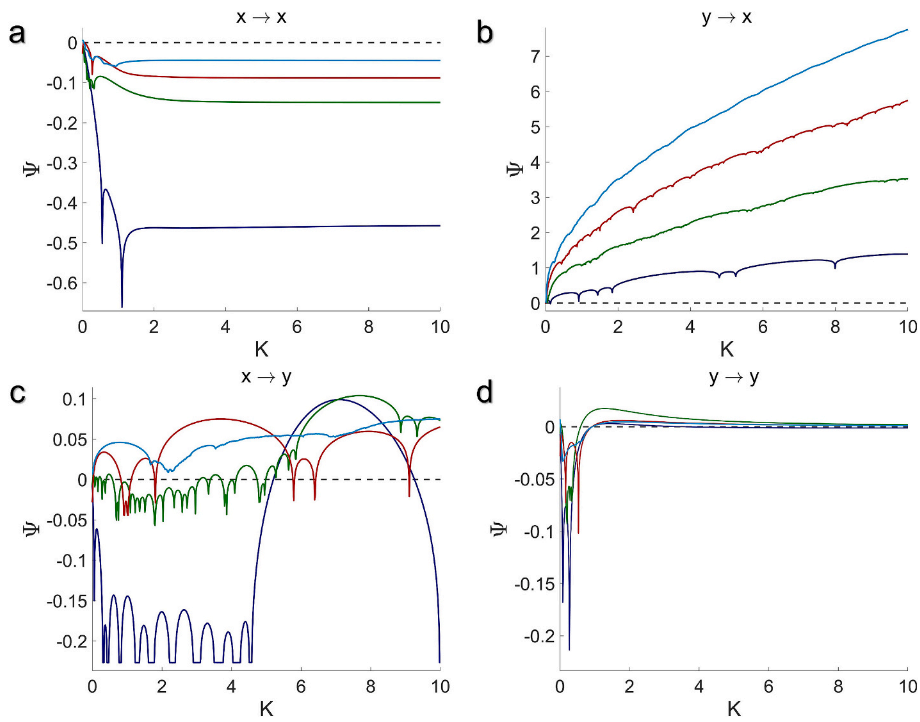

Fig. 11. MSF, defined as the maximum transverse Lyapunov exponent $\Psi(K)$, for the forced mixed tanh–exponential oscillator (variational System 16, $A = 2.7$) over the normalized coupling strength range $0 \leq K \leq 10$. The four panels correspond to the four single-variable coupling configurations: **(a)** $x\to x$, **(b)** $y\to x$, **(c)** $x\to y$, and **(d)** $y\to y$. Each colored curve represents the MSF evaluated on a specific coexisting attractor (synchronization manifold) selected by the initial conditions $X_0 = [x_0, 0]^T$, with $x_0 \in \{2, 10, 15, 25\}$, matching the colors of the attractors in Fig. 9b. The overall stability trends are largely preserved compared to the unforced case (Fig. 10) for $x\to x$, $y\to x$, and $y\to y$ couplings. However, under the $x\to y$ coupling (panel c), the forcing severely degrades synchronizability: the innermost manifold develops a broad positive lobe, and the other manifolds show enlarged unstable regions, indicating that forcing fragments the stability windows in this configuration.

4. Conclusions

This work investigated synchronization in megastable systems by applying the master-stability framework across multiple coexisting attractors and coupling channels. Across three representative oscillators, we found that synchronization is strongly attractor-dependent and channel-specific. Inner attractors—typically more dissipative—support wider and more robust stability ranges, whereas outer, less-dissipative attractors exhibit weaker or lost synchrony. The broadcast channel (e.g., which state is coupled into which equation) decisively shapes the attainable synchronization regime, often more than the coupling magnitude itself.

External forcing enriches the local dynamics (periodic, quasiperiodic, and chaotic responses) but does not uniformly enhance synchronizability. In several instances, forcing preserved the qualitative MSF pattern; in others, it fragmented stability into narrow windows or shifted it to low-K neighborhoods. These outcomes underline a key principle: in megastable settings, dissipativity and

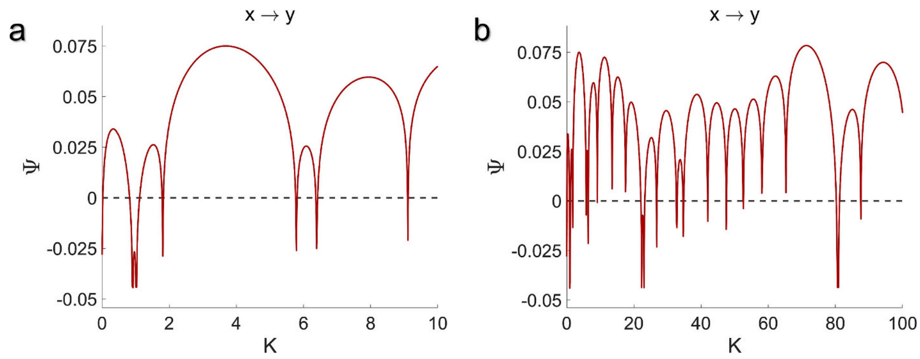

Fig. 12. Extended analysis of the MSF $\Psi(K)$ for the third attractor (red curve in Fig. 9b) of the forced mixed tanh–exponential oscillator (variational System 16, $A = 2.7$) under the $x{\to}y$ coupling configuration. The plots show $\Psi(K)$ over two different coupling ranges: **(a)** $0 \le K \le 10$ and **(b)** $0 \le K \le 100$. The initial condition used is $X_0 = [15, 0]^T$. Unlike the previous cases where the MSF eventually stabilized, this plot reveals that the oscillatory structure with frequent zero-crossings persists over the entire extended range up to $K = 100$. This indicates that the synchronization manifold remains highly sensitive to coupling variations, and the extremely narrow, scattered stability windows render the system effectively unsynchronizable in networks with broad Laplacian spectra. (For interpretation of the references to colour in this figure legend, the reader is referred to the web version of this article.)

signal routing through the coupling function govern collective behavior more than any single parameter.

A central and unexpected finding is the appearance of MSF curves with numerous zero-crossing points that persist over broad coupling ranges. This oscillatory pattern—rare in the literature—implies recurrent transitions between stability and instability, making global synchronization practically unattainable for networks with widely spread Laplacian spectra. In such cases, even small mismatches in effective coupling across modes prevent all eigenmodes from lying in the same stability interval. Regarding the generalizability of these findings, it is important to clarify that the emergence of such specific oscillatory MSF patterns may not be a universal feature of all megastable systems. Whether this phenomenon is fundamentally associated with megastability itself or strictly tied to the specific dynamical structures of the benchmark oscillators analyzed here requires further investigation across a broader variety of megastable systems. Additionally, our observations indicate that the pronounced oscillatory behaviors predominantly emerge for the inner attractors. Whether similar behaviors could emerge for attractors farther from the origin and how this specifically relates to the spatial decrease in dissipativity can be investigated in a future study.

Furthermore, our analysis reveals that the highly fragmented oscillatory MSF patterns with numerous zero-crossings predominantly emerged under specific cross-coupling configurations (e.g., $x{\to}y$ or $y{\to}x$). Under self-coupling ($x{\to}x$ or $y{\to}y$), the MSF curves typically remained monotonic or exhibited broad, contiguous stability windows. However, it is important to note that this is an observed result specific to the dynamics and coupling matrices analyzed in this study, rather than an inherent mathematical rule. Whether this strong dependence on cross-coupling is an inherent feature of megastable systems in general or strictly tied to the specific nonlinearities of the benchmark oscillators analyzed here requires further investigation across a broader variety of megastable and general nonlinear systems.

Our observations also indicate that the pronounced oscillatory MSF patterns—specifically the multiple zero-crossings that fragment the stability windows—mostly emerge and become significantly more severe after the external forcing term is introduced. Importantly, in the forced regime, these oscillatory patterns are observed for both chaotic and periodic (or quasiperiodic) manifolds. This demonstrates that the oscillatory MSF behavior is not an exclusive signature of chaotic dynamics, but rather a general feature arising from the interplay between the external forcing, the megastable local dynamics, and the specific coupling channels.

While the MSF framework is highly effective for megastable systems with discrete attractors, its direct application to extreme multistability presents fundamental challenges. In extreme multistability, an uncountable continuum of attractors coexists, resulting in a continuous dependence on initial conditions. Consequently, the complete synchronous manifold is highly fragile; any infinitesimal perturbation causes the oscillators to drift onto different attractors. Therefore, while it is theoretically possible to formulate and compute the MSF for such systems, the continuous nature of the attractor family ensures that any infinitesimal perturbation will cause the oscillators to drift apart, rendering complete synchronization practically unachievable.

Moreover, the specific oscillatory MSF patterns reported here are highly sensitive to the chosen coupling function. This study focused on linear diffusive coupling due to its physical relevance and standard role in the MSF framework. Employing other coupling schemes, such as nonlinear or delayed functions, would modify the variational equations and inevitably alter the resulting MSF curves. Investigating how different coupling architectures interact with the infinite coexisting attractors of megastable systems remains a compelling direction for future research.

The practical implication of these repeated stability-instability transitions is that real-world networks operating in these regimes will struggle to maintain global synchrony. Instead of a smooth transition to a coherent state, slight parameter mismatches or noise will cause the network to experience an intermittent loss of coherence or chaotic itinerancy between synchronized and desynchronized states. Consequently, identifying and avoiding these oscillatory MSF regimes is crucial for ensuring robust network operation.

These findings hold significant potential for applications in neuromorphic computing, where selectively synchronizing specific attractors could be harnessed for multi-task memory storage, as well as in critical infrastructure like power grids, where avoiding fragmented stability is essential. However, a key limitation of this study is its restriction to linear diffusive coupling and identical benchmark oscillators. Future research must extend these findings to heterogeneous networks and complex coupling mechanisms to fully capture real-world complexities.

Overall, the study delineates how megastability reshapes classical expectations about network synchronization: stability depends not only on "how much" the oscillators are coupled, but also on which attractor is selected and how the coupling injects information. These insights inform the design and control of multistable networks, suggesting that reliable synchrony, when possible, requires careful selection of initial conditions, coupling architecture, and forcing amplitude. Future work could extend these results to heterogeneous networks, time-varying or adaptive couplings, and experimental realizations where the narrow stability windows discovered here are especially consequential.

CRediT authorship contribution statement

Karthikeyan Rajagopal: Writing – original draft, Methodology, Formal analysis. **Arezoo Firouzeh:** Writing – original draft, Visualization, Investigation. **Mahtab Mehrabbeik:** Writing – original draft, Visualization, Software. **Sajad Jafari:** Writing – review & editing, Supervision, Conceptualization. **Julien Clinton Sprott:** Writing – review & editing, Validation, Supervision.

Declaration of competing interest

The authors declare that they have no known competing financial interests or personal relationships that could have appeared to influence the work reported in this paper.

Data availability

No data was used for the research described in the article.

References

[1] Arenas A, Díaz-Guilera A, Kurths J, Moreno Y, Zhou C. Synchronization in complex networks. Phys Rep 2008;469(3):93–153. https://doi.org/10.1016/j.physrep.2008.09.002.
[2] Lv M, Ma J, Yao Y, Alzahrani F. Synchronization and wave propagation in neuronal network under field coupling. Sci China Technol Sci 2019;62(3):448–57. https://doi.org/10.1007/s11431-018-9268-2.
[3] Tang Y, Qian F, Gao H, Kurths J. Synchronization in complex networks and its application – a survey of recent advances and challenges. Annu Rev Control 2014;38(2):184–98. https://doi.org/10.1016/j.arcontrol.2014.09.003.
[4] Yu F, He S, Yao W, Cai S, Xu Q. Bursting firings in memristive Hopfield neural network with image encryption and hardware implementation. IEEE Trans Comput-Aided Des Integr Circuits Syst 2025:1. https://doi.org/10.1109/TCAD.2025.3567878.
[5] Shahriari Z, Algar SD, Walker DM, Small M. Synchronization detection using spatial ordinal partitions in networks. Phys Rev E 2025;112(6):064206. https://doi.org/10.1103/9chy-4db8.
[6] Weng T, Chen X, Ren Z, Yang H, Zhang J, Small M. Synchronization of multiple mobile reservoir computing oscillators in complex networks. Chaos, Solitons Fractals 2023;177:114217. https://doi.org/10.1016/j.chaos.2023.114217.
[7] Ma J, Li F, Huang L, Jin W-Y. Complete synchronization, phase synchronization and parameters estimation in a realistic chaotic system. Commun Nonlinear Sci Numer Simul 2011;16(9):3770–85. https://doi.org/10.1016/j.cnsns.2010.12.030.
[8] Ma J, Mi L, Zhou P, Xu Y, Hayat T. Phase synchronization between two neurons induced by coupling of electromagnetic field. Appl Math Comput 2017;307:321–8. https://doi.org/10.1016/j.amc.2017.03.002.
[9] Shahverdiev EM, Sivaprakasam S, Shore KA. Lag synchronization in time-delayed systems. Phys Lett A 2002;292(6):320–4. https://doi.org/10.1016/S0375-9601(01)00824-6.
[10] Sorrentino F, Pecora LM, Hagerstrom AM, Murphy TE, Roy R. Complete characterization of the stability of cluster synchronization in complex dynamical networks. Sci Adv 2016;2(4):e1501737. https://doi.org/10.1126/sciadv.1501737.
[11] Abrams DM, Strogatz SH. Chimera states for coupled oscillators. Phys Rev Lett 2004;93(17):174102. https://doi.org/10.1103/PhysRevLett.93.174102.
[12] Li X, Ghosh D, Lei Y, Small M. Synchronization and chimera states in time-varying multilayer networks with higher-order interactions. Chaos 2025;35(5):053148. https://doi.org/10.1063/5.0258367.
[13] Pecora LM, Carroll TL. Master stability functions for synchronized coupled systems. Phys Rev Lett 1998;80(10):2109–12. https://doi.org/10.1103/PhysRevLett.80.2109.
[14] Mehrabbeik M, Jafari S, Parastesh F. Synchronization in a memristive duplex network: the impact of intra-layer and inter-layer synaptic pathways. Phys Lett A 2025;530:130112. https://doi.org/10.1016/j.physleta.2024.130112.
[15] Hu X, Wu Y, Ding Q, Huang W, Ye Z, Jia Y, et al. Inter-layer, intra-layer and complete synchronization in multiplex neuron networks. Nonlinear Dyn 2025;113(16):21813–32. https://doi.org/10.1007/s11071-025-11266-1.
[16] Pal PK, Anwar MS, Perc M, Ghosh D. Global synchronization in generalized multilayer higher-order networks. Phys Rev Res 2024;6(3):033003. https://doi.org/10.1103/PhysRevResearch.6.033003.
[17] Mehrabbeik M, Jafari S, Perc M. Synchronization in simplicial complexes of memristive Rulkov neurons. Front Comput Neurosci 2023;17:1248976. https://doi.org/10.3389/fncom.2023.1248976.
[18] Mehrabbeik M, Ahmadi A, Bakouie F, Jafari AH, Jafari S, Ghosh D. The impact of higher-order interactions on the synchronization of Hindmarsh–Rose neuron maps under different coupling functions. Mathematics 2023;11(13):2811. https://doi.org/10.3390/math11132811.
[19] Gambuzza LV, Di Patti F, Gallo L, Lepri S, Romance M, Criado R, et al. Stability of synchronization in simplicial complexes. Nat Commun 2021;12(1):1255. https://doi.org/10.1038/s41467-021-21486-9.
[20] Sun H, Cao H. Complete synchronization of coupled Rulkov neuron networks. Nonlinear Dyn 2016;84(4):2423–34. https://doi.org/10.1007/s11071-016-2654-z.
[21] Rakshit S, Ray A, Bera BK, Ghosh D. Synchronization and firing patterns of coupled Rulkov neuronal map. Nonlinear Dyn 2018;94(2):785–805. https://doi.org/10.1007/s11071-018-4394-8.
[22] Hu D, Cao H. Stability and synchronization of coupled Rulkov map-based neurons with chemical synapses. Commun Nonlinear Sci Numer Simul 2016;35:105–22. https://doi.org/10.1016/j.cnsns.2015.10.025.

[23] Parastesh F, Rajagopal K, Jafari S, Perc M, Schöll E. Blinking coupling enhances network synchronization. Phys Rev E 2022;105(5):054304. https://doi.org/10.1103/PhysRevE.105.054304.
[24] Kohar V, Ji P, Choudhary A, Sinha S, Kurths J. Synchronization in time-varying networks. Phys Rev E 2014;90(2):022812. https://doi.org/10.1103/PhysRevE.90.022812.
[25] Ghosh D, Banerjee S. Adaptive scheme for synchronization-based multiparameter estimation from a single chaotic time series and its applications. Phys Rev E 2008;78(5):056211. https://doi.org/10.1103/PhysRevE.78.056211.
[26] Dayani Z, Parastesh F, Jafari S, Schöll E, Kurths J, Sprott JC. Similar master stability functions for different coupling schemes in basic chaotic systems. Int J Bifurcat Chaos 2023;33(10):2350122. https://doi.org/10.1142/S0218127423501225.
[27] Mirzaei S, Anwar MS, Parastesh F, Jafari S, Ghosh D. Synchronization in repulsively coupled oscillators. Phys Rev E 2023;107(1):014201. https://doi.org/10.1103/PhysRevE.107.014201.
[28] Panahi S, Nazarimehr F, Jafari S, Sprott JC, Perc M, Repnik R. Optimal synchronization of circulant and non-circulant oscillators. Appl Math Comput 2021;394:125830. https://doi.org/10.1016/j.amc.2020.125830.
[29] Bao BC, Li QD, Wang N, Xu Q. Multistability in Chua's circuit with two stable node-foci. Chaos 2016;26(4):043111. https://doi.org/10.1063/1.4946813.
[30] Chen B, Xu Q, Chen M, Wu H, Bao B. Initial-condition-switched boosting extreme multistability and mechanism analysis in a memcapacitive oscillator. Front Inf Technol Electron Eng 2021;22(11):1517–31. https://doi.org/10.1631/FITEE.2000622.
[31] Bao BC, Bao H, Wang N, Chen M, Xu Q. Hidden extreme multistability in memristive hyperchaotic system. Chaos, Solitons Fractals 2017;94:102–11. https://doi.org/10.1016/j.chaos.2016.11.016.
[32] Sprott JC, Jafari S, Khalaf AJM, Kapitaniak T. Megastability: coexistence of a countable infinity of nested attractors in a periodically-forced oscillator with spatially-periodic damping. Eur Phys J Spec Top 2017;226(9):1979–85. https://doi.org/10.1140/epjst/e2017-70037-1.
[33] Jafari S, Rajagopal K, Hayat T, Alsaedi A, Pham V-T. Simplest Megastable chaotic oscillator. Int J Bifurcat Chaos 2019;29(13):1950187. https://doi.org/10.1142/S0218127419501876.
[34] Ramakrishnan B, Faghani Z, Natiq H, Pal N, Nazarimehr F, Jafari S. A megastable oscillator with two types of attractors. Sci Iran 2025;32(5):6909. https://doi.org/10.24200/sci.2022.60637.6909.
[35] Huang L, Chen Q, Lai Y-C, Pecora LM. Generic behavior of master-stability functions in coupled nonlinear dynamical systems. Phys Rev E 2009;80(3):036204. https://doi.org/10.1103/PhysRevE.80.036204.
[36] Wolf A, Swift JB, Swinney HL, Vastano JA. Determining Lyapunov exponents from a time series. Physica D 1985;16(3):285–317. https://doi.org/10.1016/0167-2789(85)90011-9.